Detection of Small Fiber Neuronal Activity with Optically Pumped Magnetometers

Yifeng Bu, Amir Borna, Peter Schwindt, Xiangjian Zeng, Elizabeth Baum, Ramesh Rao, Donald Kimball, Vishal Shah, Todd Coleman, Mingxiong Huang, Imanuel Lerman

Abstract*— The pain experience is a complex process that involves the activation of multiple neuronal signaling pathways that originate in the peripheral nervous system and are transmitted to the central nervous system. In the peripheral nervous system, specialized peripheral nociceptor (unmyelinated C fibers and lightly myelinated Aδ fibers) depolarization results in afferent transmission of noxious signals. Small Fiber Neuropathy (SFN) can result in chronic neuropathic pain with significant lifetime morbidity if not promptly treated. Current technological and operator limitations may delay SFN diagnosis and prolong appropriate treatment. Therefore, there is an unmet need for robust and non-invasive ways to accurately measure small fiber function. It is well known that the propagation of action potentials along a nerve is the result of ionic current flow which, according to Ampere's Law, generates a small magnetic field that is detectable by magnetometers such as superconducting quantum interference device (SQUID) Magnetoencephalography (MEG) systems. Optically pumped magnetometers (OPM) are an emerging class of quantum magnetic sensors with a demonstrated sensitivity of 1 fT/√Hz level, capable of cortical action potential detection. However, they have not as of yet been implemented for peripheral nerve action potential detection. We demonstrate for the first time, compelling evidence that OPMs can detect the magnetic signature of travelling peripheral nerve action potentials that indicate OPM's use as a potential technique for SFN diagnosis.

***Index Terms*— Median Nerve Action Potential, Optically Pumped Magnetometer (OPM), Small Fiber Neuropathy (SFN).**

Manuscript submitted Jan 14, 2021. This work was supported by Biological Advanced Research and Development Authority (BARDA) Contract# 75A50119C0038. *(Corresponding author: Imanuel Lerman, e-mail: ilerman@health.ucsd.edu)*

Y. Bu, X. Zeng, E. Baum, R. Rao, D. Kimball, and I. Lerman are with the Department of Electrical and Computer Engineering, University of California, San Diego, CA 92093, USA

A. Borna and P. Schwindt are with the Sandia National Laboratories, PO Box 5800, Albuquerque, NM 87185-1082, USA

T. Coleman is with the Department of Bioengineering, University of California, San Diego, CA, 92093, USA

M. Huang is with the Department of Radiology, University of California, San Diego, CA 92093, USA

V. Shah is with QuSpin Inc., PO Box 5800, Albuquerque, NM 87185-1082, USA

I. Introduction

THE human peripheral nervous system is composed of an intricate network of motor, sensory and autonomic neural structures [1-3]. Pain and touch integrate both nociceptor (small fibers; Aδ, C) as well as light and deep pressure proprioceptor (large fibers; Aα Aβ) transmission [4-6]. Disease of the peripheral nerves is termed Peripheral Neuropathy [7]. Small Fiber Peripheral Neuropathy (SFN) primarily affects unmyelinated (C) or lightly myelinated (Aδ) fibers [8]. Current state of the art SFN multimodal non-invasive (Quantitative Sensory Testing, Quantitative Sudomotor Axon Reflex Testing) and invasive (Microneurography, Skin Punch Biopsy) diagnostic modalities both show low sensitivity (from 45-88%) [9]. Additional invasive diagnostics such as needle-based Nerve Conduction Studies (NCS) are only capable in identification of large fiber peripheral nerve disease. These techniques can also demonstrate high variability (due to equipment and operator limitations) while they are uniformly incapable of identifying small fiber action potentials [10]. Invasive skin punch biopsies have somewhat improved diagnostic SFN sensitivity and specificity; however, they can result in significant patient discomfort that inevitably limits their widespread use [11, 12]. Microneurography using a tungsten microelectrode inserted into the small fiber of interest can demonstrate small fiber activity-dependent slowing of conduction velocity or spontaneous small fiber discharge, but diagnostic accuracy is highly operator dependent [13, 14]. Lastly, non-invasive diagnostic methods, such as quantitative sensory testing, rely on the subjective patient report that commonly contradict test accuracy and reliability, contributing to reported low test sensitivity [15, 16]. As such, there is an unmet need to improve accurate SFN diagnostics in an effort to hasten early treatment and improve morbidity associated with SFN.

Super conducting quantum interference devices (SQUID) sensor arrays are non-invasive diagnostic employed to detect cortical neuronal action potentials with magnetoencephalography (MEG). Peripheral nerve action potentials in the human wrist (median nerve) [17, 18] and more recently, in the dorsal root ganglion and spinal cord, have successfully been detected with SQUID sensor arrays [19]. Highly sensitive SQUID sensors can detect femtotesla magnetic fields typically generated by neuronal action potentials. Lang et.al. (1998) successfully captured ulnar nerve fast fiber action potentials using SQUID sensors [17].

However, conventional SQUID sensor use is highly limited, as it requires cryogenic temperature provided with liquid helium (4 K or -269 °C) and magnetically shielded rooms (MSRs). Moreover, SQUID sensors are housed in a rigid dewar which prohibit adjacent placement to the peripheral nerve (i.e., upper and lower extremity limb) that inherently requires highly mobile and conformal sensor arrays.

In comparison to currently available Peripheral Neuropathy diagnostics, OPM sensors are conformal with a 6.5mm sensor stand-off that in aggregate contribute to a magnetic sensitivity that surpasses current SQUID sensor technology. Hence, OPMs are a prime candidate for non-invasive peripheral nerve diagnostics. Nonetheless OPMs still require operation in a magnetically shielded room. In brief, OPMs employ light-atom interaction to detect magnetic fields. OPM sensors operating in the spin-exchange-relaxation-free (SERF) regime have demonstrated a sensitivity of less than 1 fT/√Hz [20] and are commercially available [21]. In SERF OPMs, a tuned laser light passes through the alkali atoms, e.g. rubidium (^{87}Rb), contained in a glass cell and optically pumps [22] the atoms into a magnetically sensitive state. By changing the coherence of the alkali atoms' atomic spins, the external magnetic field alters the intensity of the transmitted light, passing through the atoms. A photodetector senses the light intensity, proportional to the atoms' transparency, and converts the light intensity to electrical current [23].

Recently Broser et.al., (2019) [24, 25] showed that commercial Gen-1 OPMs (QuSpin Inc, CO, USA) can be used to detect compound muscle action potentials consistent with motor neuron activation. Expounding on this work, we employed the commercially available Gen-2 OPMs (QuSpin Inc, CO, USA) to measure upper extremity sensory nerve action potentials. We hypothesized that the highly sensitive OPM could be leveraged to measure peripheral nerve action potentials in the human upper extremity. To test this hypothesis, we employed OPM as a non-painful, non-invasive, reusable, and flexible diagnostic platform aimed to measure peripheral nerve action potentials.

II. Methods

A. Experimental Setup and Procedures

The Institutional Review Board at the University of California San Diego (UCSD) Health Systems approved the experimental protocol (UCSD IRB:171154). Four healthy male subjects (age: 28±10 years) without history, signs, or symptoms of neuropathy, gave their written consent. On the visit day, OPM-based peripheral nerve measurements were carried out within the UCSD Radiology Imaging Laboratory's six-layer MSR (IMEDICO, Switzerland), to minimize powerline noise and the Earth magnetic field. The employed MSR has a shielding factor of 65-160 dB for the 0.01 Hz-10 Hz frequency range. Subjects were asked to remove all electronic equipment and metal accessories before entering the MSR to avoid magnetic noise and sensor saturation.

Subjects were comfortably seated in an adjustable plastic chair (Elekta-Neuromag, Sweden) centered in the middle of the MSR. A pillow was positioned below the subject's elbow to ensure comfortable yet maximal extension of the arm. A 20 MHz portable ultrasound transducer (Butterfly IQ, Palo Alto, USA) was used to measure the median nerve's depth, circumference, and area at both distal (wrist) and proximal (forearm) sites. The proximal antecubital fossa was selected as the antidromic stimulation site with a pair of bipolar stimulation electrodes (Fig. 1a, 2a). Proximal forearm and distal wrist sites were selected for neuronal action potential measurements to allow for accurate measures of temporal dispersion (Fig. 1a, 2a). All subjects underwent left arm antecubital fossa median nerve stimulation with the DS7AH constant current stimulator (Digitimer Ltd, UK) using a 1 Hz, 200 μs pulse-width, monopolar square-wave [26]. The protocol for Aδ fiber activation was derived from Mackenzie et al (1975), in which 1 Hz upper extremity peripheral nerve stimulation intensity was slowly increased to produce a sharp pinprick sensation resulting in a reproducible Aδ fiber nerve conduction velocity of 12-15 m/s [27, 28]. The antecubital fossa median nerve was visualized with B-mode ultrasound imaging and marked for electrical stimulator placement. Stimulation current was incrementally adjusted to just above sensory threshold (sharp pinprick sensation on the anterior palm including first and second fingers) with assurance of unobservable muscle activation in the forearm and hand. Nerve conduction velocity was calculated with standardized clinical sensory nerve action potential methods [10, 26, 29, 30], in which the distance (i.e., 70 mm) between two measurement sites (proximal forearm and the distal wrist) is divided by the temporal dispersion (6 ms) at each site.

Four modified Gen2 OPMs were used to measure median nerve action potentials. In comparison to the Gen-1 OPM (dimensions: 13.0×19.0×110.0 mm^3), Gen-2 OPMs have a significantly smaller footprint (12.4×16.6×24.4 mm^3) that improves conformal placement of the OPM array. Gen-2 OPMs demonstrate improved sensitivity (7-10 fT/√Hz) and have an extended tolerance to background magnetic field (up to 200 nT) while maintaining ±5 nT dynamic range [31]. The modified OPM were operated in single-axis mode.

Conventional surface electrodes were first carefully positioned over the median nerve at both the proximal (forearm) and distal (wrist) location [32] as identified by ultrasound scan. Active gold-plated surface electrodes (Technomed Europe, Netherlands) were placed at the wrist and the forearm median nerve site (with a 7 cm proximal to distal separation) while reference electrodes were placed distally to the active electrodes. In all measurements, the ground electrode was placed at the ulnar notch of the radial bone. EC3 Grass conductive adhesive gel (Natus, Pleasanton, CA, USA) was applied to each electrode cup with assurance of impedance maintenance at 5000 Ω or less.

To match surface electrode time-locked measurements, a single OPM was secured with a conformal Velcro strap positioned at the identical site of the conventional electrode site over the median nerve (identified with ultrasound scan) in the longitudinal position (i.e., at the distal wrist and proximal forearm). The Z-direction of the OPM was adjusted normal to the skin surface in the longitudinal direction along the nerve.

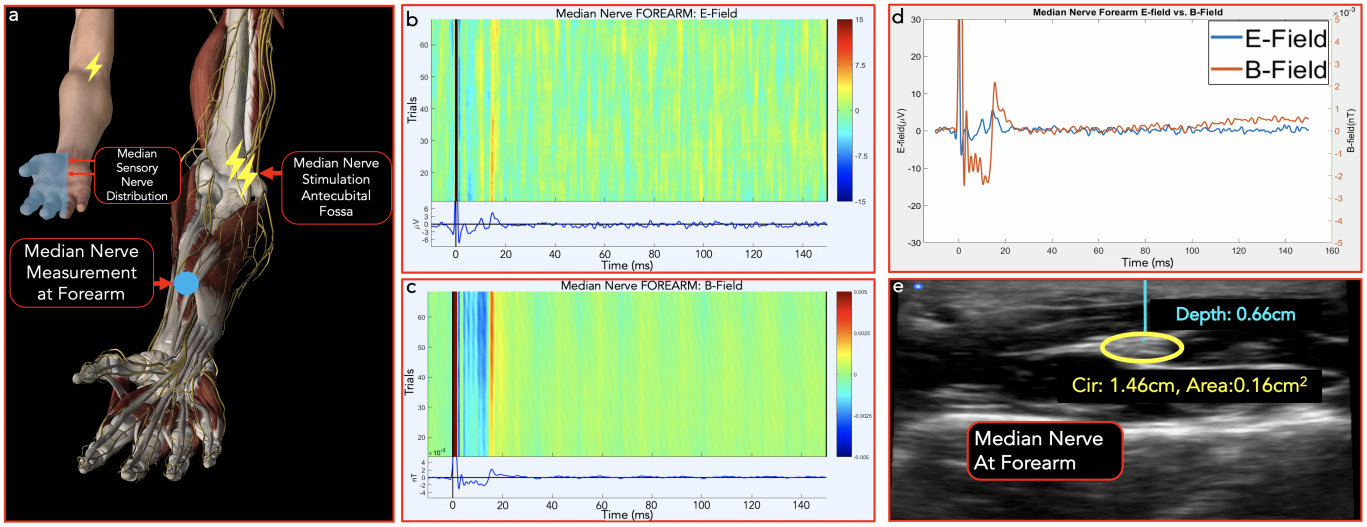

Fig. 1. Median nerve sensory distribution (shaded blue) activated with electrical stimulation at the antecubital fossa. Median nerve action potential measures were carried out with Optically Pumped Magnetometers and conventional surface electrodes at the anterior Forearm. b) ERP plot of wrist E-field measurement with conventional surface electrodes. c) ERP plot of forearm B-field measurement by OPMs. d) Time-locked average comparison between E-field and B-field. e) Transverse B-mode ultrasound imaging at forearm. Median nerve depth: 0.66cm (blue line); circumference: 1.46cm; Area: 0.16cm² (yellow circle). OPM = Optically Pumped Magnetometers, ERP= Event Related Potentials, E-Field = Electric Field, B-Field = Magnetic Field, Cir = Circumference.

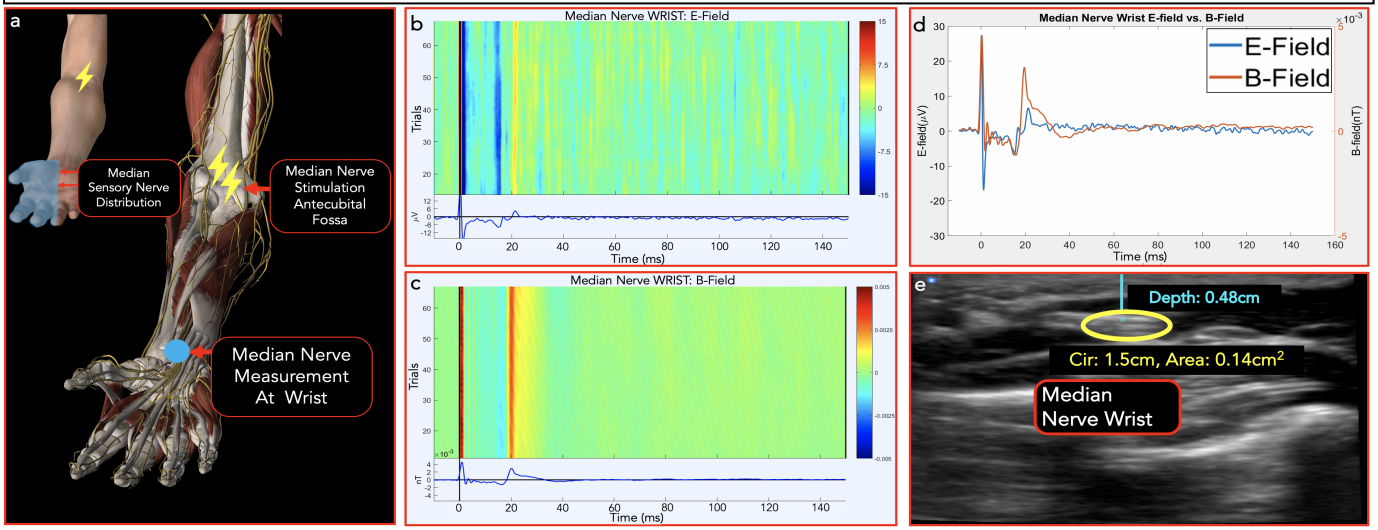

Fig. 2. Median nerve measurement at wrist. a) Median nerve sensory distribution (shaded blue) activated with electrical stimulation at the antecubital fossa (yellow lightning bolt). Median nerve action potential measures were carried out with Optically Pumped Magnetometers and conventional surface electrodes at the anterior Wrist. b) ERP plot of wrist E-field measurement with conventional surface electrodes. c) ERP plot of wrist B-field measurement with OPM. d) Wrist Time-locked average comparison between E-field and B-field. d) ERP plot of wrist B-field measurement by OPM. e) Transverse B-mode ultrasound imaging at wrist. Median nerve depth: 0.48cm (blue line); circumference: 1.5cm (yellow circle); Area: 0.14cm². OPM = Optically Pumped Magnetometers, ERP= Event Related Potentials, E-Field = Electric Field, B-Field = Magnetic Field, Cir = Circumference.

To further confirm the source of the detected action potential and to measure the nerve signal conduction, 3 OPM sensors were placed in transverse orientation to the median nerve at both proximal (forearm) and distal (wrist) locations. (Fig. 3b, 3d). The central OPM sensor was placed directly over the proximal and distal median nerve confirmed with ultrasound scan. The two remaining OPMs were positioned radially 3 cm lateral and medial to the central OPM sensor at the equipotential level. We employed notch filters to remove powerline and harmonic noise on the 3 sensor measurements.

In a final test to assess the spatial falloff of the nerve magnetic field in the medial-lateral direction using OPM, we employed 4 OPM sensors positioned in a transverse equipotential orientation relative to the distal median nerve at the wrist. Each of the four OPM sensors (lateral, central, medial-1, and medial-2) were separated by 2 cm in the radial orientation (Fig. 4).

B. Processing Pipeline

Electric Field (E-field) nerve conduction studies were carried out with 1 Hz sensory median nerve stimulation. The recorded skin electrode signal was amplified and bandpass filtered from 2-2000 Hz using a Digitimer D360 isolated amplifier (Digitimer Ltd, UK), sampled by a CED Micro1401 device at 10 kHz, and recorded by Signal 8.19a software (Cambridge Electronic Design, Cambridge, UK). A HumBug single-channel Noise Eliminator (Quest Scientific, North Vancouver BC, Canada) was connected between the amplifier

and data acquisition system to eliminate the 60 Hz powerline and harmonic noise. The HumBug eliminator constructs a noise replica in real time and continuously subtracts this replica from the input signal without waveform distortion [33]. All stimuli were repeated 70 times with a time-locked trigger to enable trial averaging of all event related potentials (ERPs), while no trial rejection was necessary due to high signal to noise ratio.

Prior to OPM neuronal recordings, each OPM was tuned and calibrated in an absolute zero magnetic field environment in the closed door MSR with the OPM gain set to 2.7 V/nT. The modified Gen 2 OPMs were enabled with effective bandwidth up to 500 Hz and a second order Butterworth 20-500 Hz bandpass filter was applied [34], before the ERP averaging to eliminate body drift effects and other high frequency noise sources. All post processing was carried out with MATLAB software (MathWorks Inc, MA, USA). ERP plots were constructed and plotted in EEGLAB package (EEGLab, San Diego, CA USA) [35] with the aim to display robust, repeatable action potential recordings.

Conventional clinical sensory nerve action potential (SNAP) filtering techniques commonly employ 2-2000 Hz cut off frequency known to capture 2-4 ms spike resolution with repeated stimuli [36]. With Gen 2 OPM 500 Hz bandwidth enabled we employed a 20-500 Hz cut off frequency and a 60 Hz notch filter aimed to emulate conventional clinical SNAP acquisition and reduce noise interference.

With a minimal 4 OPM Sensor requirement, independent component analysis (ICA) was employed to maximize the signal to noise ratio. ICA first decomposes multi-channel signals into independent sources. After identifying and removing the interference components (i.e. stimulation artifact and powerline noise) from the raw measurements, the continuous OPM data was then reconstructed from the remaining ICA components. Prior to ICA the 60Hz notch filter was removed to reduce data distortion and signal oscillation and to allow for ICA 60 Hz noise component removal. The FieldTrip toolbox for MATLAB was used to implement the ICA algorithm [37].

III. Results

A. Ultrasound Neural Imaging Measurements

Using high resolution B-mode ultrasound imaging, we accurately measured the median nerve circumference, area and depth at the wrist and forearm (Fig. 1e, Fig 2e). the median nerve measured at the proximal forearm and distal wrist was similar in circumference (1.46 cm and 1.5 cm, respectively) and area (0.14 cm^2 and 0.16 cm^2, respectively) but was located deeper at the proximal forearm (0.66 cm) when compared to the wrist (0.48cm).

B. Optically Pumped Magnetometer Measurements

Three different experiments were conducted in order to verify OPM small fiber action potential detection. In our first experiment, we aimed to objectively compare median nerve action potential acquisition between the OPM and conventional surface electrode measures. Triphasic action potential peak latencies were identical in both electric field (E-field) and magnetic field (B-field) measurements at both the forearm (deflection peak at 15 ms) and wrist location (deflection peak at 21 ms) as shown in (Fig. 1b-d and 2b-d). The E-field action potential pk-pk amplitude measured at the proximal forearm (6 μV) was significantly less than the distal wrist pk-pk amplitude (12 μV). In contrast, no significant

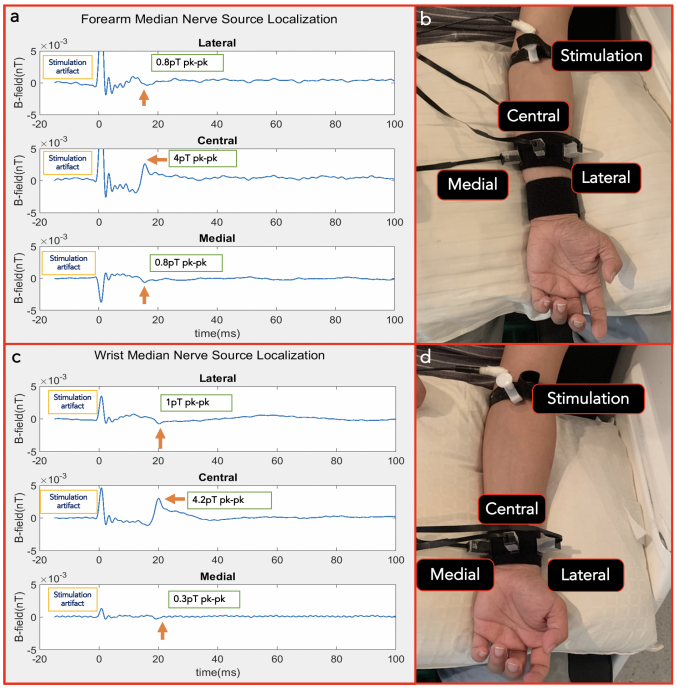

Fig. 3. 3 transversely placed OPM measurements at an equipotential level on the a) wrist and c) forearm and demonstration of the placement of 3 OPM sensors: b) wrist and d) forearm. In both experiments, the three OPMs showed consistent latency and the OPM above the median nerve had the most significant pk-pk amplitude. Electrical stimulation artifact was measured at time point 0-5 ms in both a, b.

decrease in B-field action potential amplitude was detected; we measured 4.2 pT at the distal wrist compared to 4 pT at the proximal forearm that in aggregate demonstrate a 45% improvement in signal to noise when compared to E-field measures.

In the second experiment, three radially placed OPMs were positioned at the proximal forearm and the distal wrist. The central OPM sensor placed directly above the median nerve recorded the largest amplitude action potential when measured at the distal wrist (4.2 pT pk-pk) and proximal forearm (4pT pk-pk). Both lateral and medial offset OPM sensors consistently recorded an amplitude decrement (range 0.5-1pT pk-pk) when compared to the central OPM sensor. Identical to the single sensor experiment, we observed time-locked triphasic action potentials at 15ms for the proximal forearm and at 21ms for the distal wrist in all three radially placed OPM sensors (Fig. 3a, 3c). The calculated nerve conduction velocity at 11.6m/s was consistent with that of the Aδ fiber type known to range from 5-15m/s. With 3mA antecubital fossa median nerve stimulation measured average conduction velocity (12.02 ± 3.52 m/s) was consistent across N=4 subjects.

In the third experiment, we sought to improve our spatial resolution and noise cancellation methods. To achieve this, 4 OPM sensors were placed radially at the wrist with 2cm

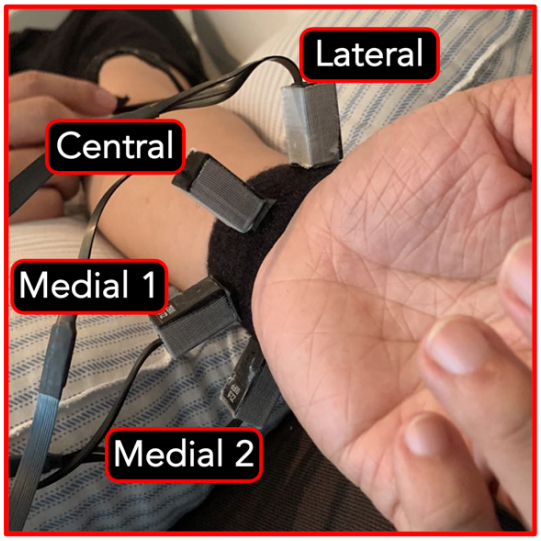

Fig. 4. 4 OPM sensors were positioned in radial orientation overlying the median nerve at the distal wrist.

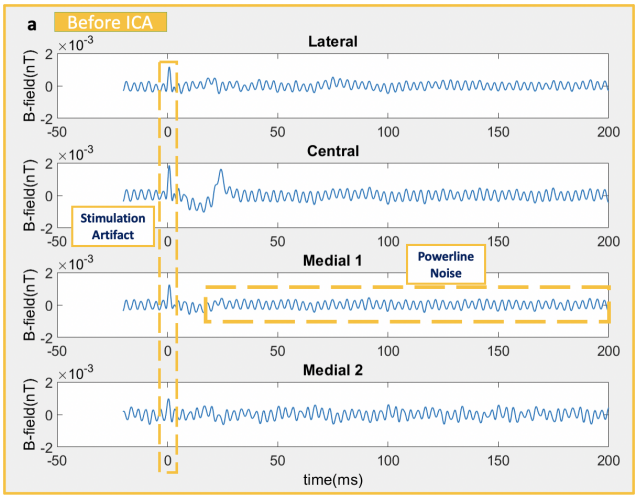

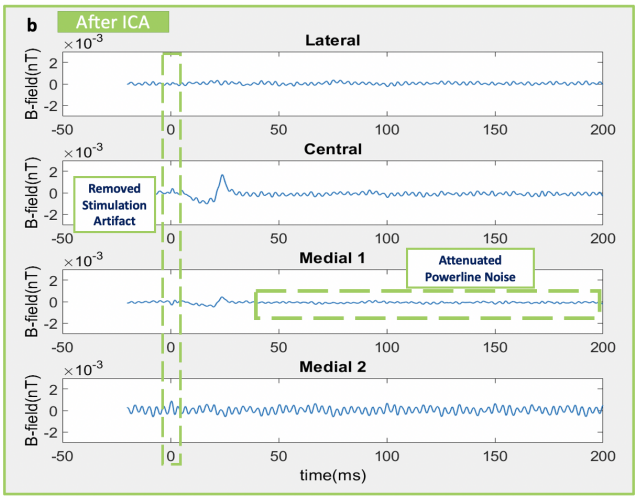

Fig. 5. 4 transversely placed OPM measurements at an equipotential level at wrist. a) before ICA processing b) after ICA processing. By running ICA, the stimulation artifact was efficiently removed, and the powerline interference was attenuated.

between each sensor in an equipotential orientation (Fig. 4). With a minimum of 4 OPM sensors required for running the ICA, the stimulation artifact and powerline noise were efficiently attenuated (Fig. 5a, 5b). The central OPM (placed directly over the identified median nerve) exhibited the largest pk-pk amplitude at 22 ms when compared to the three offset radially positioned OPMs (Fig. 5a, 5b).

The effective current density of the nerve was simulated and back-calculated by the Biot-Savart magnetic MATLAB toolbox [38] by employing the detected B-field action potential and median nerve depth to vapor cell distance (including the 6.5 mm sensor standoff). The nerve was simulated as a straight wire. The estimated total current was 0.31μA and $0.27\ \mu$A at the forearm and wrist respectively. The current density was calculated as 1.94μA/mm^2 and 1.93Aμ/mm^2 at the forearm and wrist respectively.

IV. Discussion

High fidelity electrodiagnostic tools are routinely deployed to measure neuronal action potentials and have wide utility as a peripheral nerve diagnostic. Here we demonstrate that optically pumped magnetometers are capable of high temporal and spatial resolution fiber specific peripheral nerve recordings. In aggregate, conformal OPM demonstrate potential as a sensitive, fiber-specific, clinical diagnostic device.

Three different experiments were conducted in order to verify small fiber action potential detection with OPM in the human forearm. In the first experiment, we reliably detected time-locked OPM derived triphasic action potentials that collectively demonstrate high temporal and spatial accuracy when compared to conventional electrode (E-field) measures. Similar to highly cited comparisons of EEG vs. MEG, OPM magnetic flux measures circumvent usual limitations ascribed to deep E-field recording (i.e., smearing, distortion and reduced amplitude due to higher resistive loads in deeper tissues). Collectively, the median nerve is known to be more superficial; at the wrist compared to the proximal forearm, when measured with ultrasound, MRI, and in the human cadaver [39-42]. Due to OPM inherent B-Field sensing properties (OPMs non-attenuated flux detection of deep neuronal action potentials, (i.e., the proximal forearm measured at 4 pT vs distal wrist at 4.2 pT), we show for the first time that OPMs have a superior performance profile (up to 45% improvement) when compared to conventional electrode E-field techniques.

Building on these findings in the second experiment, we confirm our capability to localize the maximal peripheral nerve action potential source by distributing three separate OPM sensors within an equipotential line at both proximal forearm and distal wrist. At both the wrist and forearm, the centrally placed OPM (directly over the ultrasound imaged median nerve) exhibited the largest pk-pk amplitude compared to the two radially placed OPM sensors. Moreover, the two off-site OPMs identified the spatial fall-off of the nerve magnetic field. Collectively, these findings verified our ability to identify a peripheral nerve action potential by employing OPM multi-sensor array methodology.

To further refine our technique and maximize our signal to noise ratio, we employed the widely used independent component analysis (ICA) method by securing four separate OPM sensors in the transverse equipotential line at the wrist level. ICA, routinely deployed for EEG and MEG decomposition into independent signal sources, allowed for

removal of biological and non-biological artifacts (i.e., electrical stimulation artifact, electrocardiogram, electrooculogram and powerline noise). In this third experiment, ICA effectively removed stimulation artifact and powerline interference while significantly improving our signal to noise ratio. The results of our third experiment, in concordance with results from the second experiment, indicate that: 1) that the central OPM (directly overlying the ultrasound imaged median nerve) exhibited the largest pk-pk amplitude and 2) the off-site OPMs identified the spatial falloff of the nerve magnetic field.

In summary, we demonstrate two major findings: 1) OPM are capable of small fiber action potential detection at both the proximal forearm (deep median nerve) and distal wrist (superficial median nerve), and 2) ICA is an effective approach to remove artifact and interference in OPM peripheral nerve recordings. In aggregate, these findings highlight the need for further study of OPM use as a non-invasive diagnostic technique for small fiber disease.

While our OPM small fiber (Aδ) neural recordings are encouraging, our work is not without limitations. First, the OPM is only operational within a MSR which limits general use in the open conventional clinic setting. Future work will focus on the development of open field capable small single limb magnetic shielding devices that may afford convenient in office OPM peripheral nerve characterization. Second, the limited bandwidth of OPMs may impede resolving short latency spike acquisition, (i.e. large fast fiber Aα and Aβ action potentials). Future work will focus on potential techniques to improve OPM bandwidth. Third, current OPMs exhibit a post electrical stimulation 0-7ms artifact described as the "ringing effect" which can obscure fast fiber action potential detection routinely recorded within the 0-7ms range. Future efforts to optimize filtering techniques of OPM transimpedance amplifier interaction with the lock-in amplifier are planned; this together may minimize the ringing effect. Lastly, accurate OPM neuronal action potential measurement required informed placement of each sensor, i.e., B-mode nerve ultrasound imaging. However, employing a multiarray 4-10 OPM sensor solution has the potential to circumvent the requirement for B-mode ultrasound scanning.

V. Conclusion

Our work demonstrates OPM can non-invasively measure peripheral nerve small fiber (Aδ) action potentials. Further, by employing an array of OPM sensors, we identified the peripheral nerve source and neural magnetic field falloff. This work opens the door to further explore OPM functionality as a non-invasive clinical diagnostic tool for small fiber nerve dysfunction.

References

1. Sulaiman, H., et al., *Presence and distribution of sensory nerve fibers in human peritoneal adhesions.* Annals of surgery, 2001. **234**(2): p. 256.
2. Mai, J.K. and G. Paxinos, *The human nervous system*. 2011: Academic Press.
3. Barr, M.L., *The human nervous system: An anatomical viewpoint*. 1974: Harper & Row.
4. Stein, R.B., *What muscle variable (s) does the nervous system control in limb movements?* Behavioral and Brain Sciences, 1982. **5**(4): p. 535-541.
5. Elvey, R.L., *Physical evaluation of the peripheral nervous system in disorders of pain and dysfunction.* Journal of hand therapy, 1997. **10**(2): p. 122-129.
6. Starr, A., *Sensory evoked potentials in clinical disorders of the nervous system.* Annual review of neuroscience, 1978. **1**(1): p. 103-127.
7. Asbury, A.K. and H.L. Fields, *Pain due to peripheral nerve damage: A hypothesis.* Neurology, 1984.
8. Hoeijmakers, J., et al., *Genetic aspects of sodium channelopathy in small fiber neuropathy.* Clinical genetics, 2012. **82**(4): p. 351-358.
9. Blackmore, D. and Z.A. Siddiqi, *Diagnostic criteria for small fiber neuropathy.* Journal of Clinical Neuromuscular Disease, 2017. **18**(3): p. 125-131.
10. Nandedkar, S.D., *Motor and sensory nerve conduction: technique, measurements, and anatomic correlation.* Neurophysiology and Instrumentation, 2010: p. 1.
11. Alport, A.R. and H.W. Sander, *Clinical approach to peripheral neuropathy: anatomic localization and diagnostic testing.* CONTINUUM: Lifelong Learning in Neurology, 2012. **18**(1): p. 13-38.
12. Lauria, G., et al., *EFNS guidelines on the use of skin biopsy in the diagnosis of peripheral neuropathy.* European journal of neurology, 2005. **12**(10): p. 747-758.
13. Serra, J., et al., *Microneurographic identification of spontaneous activity in C-nociceptors in neuropathic pain states in humans and rats.* Pain, 2012. **153**(1): p. 42-55.
14. Themistocleous, A.C., et al., *The clinical approach to small fibre neuropathy and painful channelopathy.* Practical neurology, 2014. **14**(6): p. 368-379.
15. Shy, M., et al., *Quantitative sensory testing: report of the Therapeutics and Technology Assessment Subcommittee of the American Academy of Neurology.* Neurology, 2003. **60**(6): p. 898-904.
16. Siao, P. and D.P. Cros, *Quantitative sensory testing.* Physical Medicine and Rehabilitation Clinics, 2003. **14**(2): p. 261-286.
17. Lang, G., et al., *Neuromagnetic recordings of the human peripheral nerve with planar SQUID gradiometers.* Physics in Medicine & Biology, 1998. **43**(8): p. 2379.
18. Hashimoto, I., et al., *Visualization of a moving quadrupole with magnetic measurements of peripheral nerve action fields.* Electroencephalography and Clinical Neurophysiology/Evoked Potentials Section, 1994. **93**(6): p. 459-467.
19. Adachi, Y., et al., *A SQUID system for measurement of spinal cord evoked field of supine subjects.* IEEE transactions on applied superconductivity, 2009. **19**(3): p. 861-866.

20. Kominis, I., et al., *A subfemtotesla multichannel atomic magnetometer.* Nature, 2003. **422**(6932): p. 596-599.
21. Hill, R.M., et al., *Multi-channel whole-head OPM-MEG: Helmet design and a comparison with a conventional system.* NeuroImage, 2020. **219**: p. 116995.
22. Happer, W., *Optical pumping.* Reviews of Modern Physics, 1972. **44**(2): p. 169.
23. Osborne, J., et al. *Fully integrated standalone zero field optically pumped magnetometer for biomagnetism*. in *Steep Dispersion Engineering and Opto-Atomic Precision Metrology XI*. 2018. International Society for Optics and Photonics.
24. Broser, P.J., et al., *Optically pumped magnetometers for magneto-myography to study the innervation of the hand.* IEEE Transactions on Neural Systems and Rehabilitation Engineering, 2018. **26**(11): p. 2226-2230.
25. Broser, P., et al., *Optically pumped magnetometers disclose magnetic field components of the muscular action potential.* bioRxiv, 2020.
26. NESTOR, D. and R. NELSON, *Performing motor and sensory neuronal conduction studies in adult humans.* 1990.
27. Mackenzie, R.A., et al., *Fibre function and perception during cutaneous nerve block.* Journal of Neurology, Neurosurgery & Psychiatry, 1975. **38**(9): p. 865-873.
28. Lubba, C.H., et al., *PyPNS: Multiscale simulation of a peripheral nerve in python.* Neuroinformatics, 2019. **17**(1): p. 63-81.
29. Mallik, A. and A. Weir, *Nerve conduction studies: essentials and pitfalls in practice.* Journal of Neurology, Neurosurgery & Psychiatry, 2005. **76**(suppl 2): p. ii23-ii31.
30. Kimura, J., *Principles and pitfalls of nerve conduction studies.* Annals of Neurology: Official Journal of the American Neurological Association and the Child Neurology Society, 1984. **16**(4): p. 415-429.
31. Shah, V. and M.V. Romalis, *Spin-exchange relaxation-free magnetometry using elliptically polarized light.* Physical Review A, 2009. **80**(1): p. 013416.
32. Valls-Sole, J., J. Leote, and P. Pereira, *Antidromic vs orthodromic sensory median nerve conduction studies.* Clinical neurophysiology practice, 2016. **1**: p. 18-25.
33. Scientific, Q., *Hum Bug Reference Manual.* 1997.
34. Campbell, W.W., *Essentials of electrodiagnostic medicine*. 2013: Demos Medical Publishing.
35. Delorme, A. and S. Makeig, *EEGLAB: an open source toolbox for analysis of single-trial EEG dynamics including independent component analysis.* Journal of neuroscience methods, 2004. **134**(1): p. 9-21.
36. Koo, Y.S., C.S. Cho, and B.-J. Kim, *Pitfalls in using electrophysiological studies to diagnose neuromuscular disorders.* Journal of clinical neurology (Seoul, Korea), 2012. **8**(1): p. 1.
37. Oostenveld, R., et al., *FieldTrip: open source software for advanced analysis of MEG, EEG, and invasive electrophysiological data.* Computational intelligence and neuroscience, 2011. **2011**.
38. Loic, Q., *Biot Savart magnetic Toolbox.* Tech. report, Dept. Elect. Eng., University of Applied Sciences Düsseldorf, Germany, 2015.
39. Brown, J.M., et al., *US of the peripheral nerves of the upper extremity: a landmark approach.* Radiographics, 2016. **36**(2): p. 452-463.
40. Meyer, P., et al., *The median nerve at the carpal tunnel… and elsewhere.* Journal of the Belgian Society of Radiology, 2018. **102**(1).
41. Agarwal, P., et al., *Cadaveric study of anatomical variations of the median nerve and persistent median artery at wrist.* Indian journal of plastic surgery: official publication of the Association of Plastic Surgeons of India, 2014. **47**(1): p. 95.
42. Gonzalez, N.L. and L.D. Hobson-Webb, *Neuromuscular ultrasound in clinical practice: A review.* Clinical neurophysiology practice, 2019. **4**: p. 148-163.